**Article:**
Ostorero, L., Boudon, G., Balcone-Boissard, H. et al. (7 more authors) (2025) The 1956 eruption of Bezymianny volcano (Kamchatka). Part II—Magma dynamics and timescales from crystal records. Bulletin of Volcanology, 87. 19. ISSN 0258-8900

https://doi.org/10.1007/s00445-024-01792-y

# SUPPLEMENTARY MATERIALS FOR

# The 1956 eruption of Bezymianny volcano (Kamchatka). Part II - Magma dynamics and timescales from crystal records

Lea Ostorero[1,2*], Georges Boudon[1], Hélène Balcone-Boissard[3], Caroline Martel[4], Saskia Erdmann[4], Daniel J. Morgan[5], Alexander Belousov[6], Marina Belousova[6], Vesta Davydova[7], Thiebaut d'Augustin[3]

[1]Université Paris Cité, Institut de physique du globe de Paris (IPGP), CNRS, F-75005 Paris, France

[2]Now at Department of Earth and Environmental Sciences, University of Milano-Bicocca, Milan, Italy

[3]Institut des Sciences de la Terre de Paris (ISTeP), UMR 7193, CNRS-Sorbonne Université, Paris, France

[4]Institut des Sciences de la Terre d'Orléans (ISTO), UMR 7327, Université d'Orléans-CNRS/INSU-BRGM, Orléans, France

[5]Institute of Geophysics and Tectonics, School of Earth & Environment, University of Leeds, Leeds LS2 9JT, UK

[6]Institute of Volcanology and Seismology, 9 Piip Boulevard, Petropavlovsk-Kamchatsky, 683006, Russia

[7]Lomonosov Moscow State University, Geological Departments, Leninskii Gory, 1, 119191 Moscow, Russia

# Online resource 1

## 1. Previous results by Martel et al. (accepted)

Clasts of the blast and pumiceous C-PDC are andesites with ~60 wt% $SiO_2$ and 5 wt% $Na_2O$ +$K_2O$ (recalculated with total iron as FeO and on anhydrous basis) (**Supplementary Fig. 4**) (Martel et al. accepted). The blast clasts show high vesicularity (mainly around 30-45 %), as well as the C-PDC pumices (mainly around 30-65 %) (Martel et al. accepted). The mineral assemblages of the clasts from the blast and the pumiceous C-PDC are identical and consist of plagioclase, amphibole, orthopyroxene and magnetite crystals, occurring as pheno- and micro-phenocrysts (Martel et al. accepted). The groundmass is glassy with small microlites of plagioclase mostly, as well as cristobalite in the blast clasts (Martel et al. accepted). For both the blast and pumiceous C-PDC, plagioclase crystals are euhedral and can be as long as 0.5 mm in length. Plagioclase anorthite contents ($An = \frac{Ca}{Ca+Na+K}$) are between $An_{30-77}$ for the blast clasts and $An_{50-65}$ for the C-PDC pumices (Martel et al. accepted). Amphibole crystals are euhedral and show two main populations: tschermakitic pargasite and magnesio-hornblende (Martel et al. accepted). They exhibit complex textures. Orthopyroxene crystals are also euhedral and less present than plagioclase and amphibole crystals (they are presented in more detail below). The titanomagnetite microlites are $Mt_{69-71}$ with $TiO_2$ contents of 9-10 wt% (Martel et al. accepted).

## 2. Supplementary information on the Methods

### 2.1. Sampling in the field

In the blast, samples with different lithologies, sorting and grading were collected, resulting from the sedimentation regimes of the diluted and turbulent pyroclastic density currents (PDC) (Belousov and Belousova 1998). The sample coordinates are given in **Supplementary Table 1**. **Supplementary Fig. 1** shows one of the sampling sites of the blast deposits that consists of three layers (layers A, B and C; description in the **Supplementary Fig. 1** legend) (Belousov and Belousova 1998; Belousov et al. 2007). Ten representative clasts of the blast and nine pumices from the post-blast pumiceous C-PDC (C-PDC pumices hereafter) are studied here. The Bezy 3e sub-sample comes from a block from the proximal deposit of the blast (layer B; ~3 km from the summit). The Bezy 7 and Bezy 8 samples, also from layer B, are from a trench dug ~6 km away from the summit, and contained several clasts of variable vesicularities. Blast clasts from layer B are 1-10 cm in size (Belousov et al. 2007), light grey to grey and rich in plagioclase, amphibole and pyroxene. The pumices are 1-5 cm in width, light beige in color and rich in plagioclase, amphibole and pyroxene.

| Sample | Characterization | Coordinates | Nature of the sample | d of the clast measured ($g.cm^{-3}$) (density range of all clasts) | Vesicularity of the clast (%) (vesicularity range of all clasts) | Sample preparation |
|---|---|---|---|---|---|---|
| **Bezy 3e** | Blast deposits (layer B), cryptodome (1 clast) | N55°56.465', E160°36.887' | Andesite | 1.73 (1.71-2.09) | 34.6 (21.3-34.6) | Individual opx + mgt + Rock mount |
| **Bezy 7a** | Blast deposits (layer B), cryptodome (5 clasts: Bezy 7a-66, 67, 70, 84, 86) | N55°55.068', E160° 36.910' | Andesite | 1.55-2.02 (1.14-2.42) | 24-48.7 (8.7-57.1) | Rock mounts |
| **Bezy 7b** | Blast deposits (layer B), cryptodome (2 clasts, Bezy 7b-8, 13) | N55°55.068', E160° 36.910' | Andesite | 1.08-1.53 (1.08-2.41) | 42.4-59.3 (9.2-59.3) | Rock mounts |
| **Bezy 8b** | Blast deposits (layer B), cryptodome (1 clast) | N55°55.021', E160°37.826' | Andesite | 1.61 (1.49-1.83) | 39.2 (30.1-42.6) | Rock mount |
| **Bezy 8f** | Blast deposits, (layer B), cryptodome (1 clast) | N55°55.021', E160°37.826' | Andesite | 1.57 (1.49-1.83) | 40.9 (30.1-42.6) | Opx + mgt + Rock mount |
| **Bezy 9** | Pumices: Pumiceous C-PDC (9 individual pumices; Bezy 9-17, 18, 100, 101, 102, 104, 107, 112, 114) | N55°54.987', E160°38.843' | Andesite | 1.12-1.52 (0.90-1.94) | 42.6-57.9 (26.7-66.0) | Opx + mgt + Rock mounts |

**Supplementary Table 1 Description of the 1956 climactic phase samples of Bezymianny studied here. The location, coordinates, and nature of the samples, as well as the density and vesicularity measured for the individual clasts studied here are specified. "Opx" and "mgt" stands for orthopyroxene and magnetite, respectively. The density and vesicularity ranges of all the fragments are specified (Bezy 3, Bezy 8 and Bezy 9) (from Martel et al. (accepted))**

## 2.2. Sample preparation

The unaltered andesitic samples were either used for in situ observations or crushed (up to 3 mm). Rock mounts were made in the blast deposits and pumices from the pumiceous C-PDC. For the crushed samples, one half was then crushed again into fine powder for whole rock analysis, while the other half was sieved into different size fractions (1 mm-710 µm, 710-500 µm, 500-315 µm, 315-250 µm, 250-125 µm) for crystal studies. These fractions were washed in an ultrasonic bath and dried at 80°C for 48 hours. The samples were then observed under a binocular microscope to select the fractions in which the crystals were most abundant and automorphic. Orthopyroxene, plagioclase, magnetite and amphibole crystals were then randomly hand-picked under a binocular microscope in the different selected size fractions (125 to 500 µm). Highly altered or broken crystals were discarded. They were mounted in epoxy resin and polished up to 0.3 µm to the middle of the crystals. Depending on the b- or a-axis, the color of the orthopyroxene is not the same and is clearer on the b-axis. Orthopyroxenes were then oriented by eye with the long axes (c-axis) in a north-south direction, as they have been used to model intracrystalline diffusion along the b-axis (Kilgour et al. 2014; Solaro et al. 2020; Ostorero et al. 2021; Metcalfe et al. 2021). Each mount was polished using silicon carbide polishing pads (P-800, P-1200, P-2400 and P-4000) with 0.3 µm grade aluminum powder as a final polishing step. Before scanning electron microscope (SEM) or electron microprobe micro-analyzers (EMP) investigations, selected mounts were all carbon-coated.

## 2.3. Crystals textural observations: Scanning Electron Microscope

Orthopyroxene zoned crystals were identified because they present grey levels of different intensities on back-scattered electron (BSE) images. The proportions of zoned/unzoned orthopyroxene crystals were determined for all the crystals mounted by looking closely at the SEM images. Higher resolution images (magnification x755) were taken for diffusion modelling and intercalibration with chemical profiles of orthopyroxene crystals under the same conditions as mentioned above, a high integration line (n = 7, 7 integrations of each image line to reduce the impact of noise) and a dwell time per pixel of 48 µs.

Identification of textural and possible chemical zonations in the magnetite crystals (with the presence of a melt inclusions ring (Boudon et al. 2015)) was also possible with the SEM, in order to position the rim-core profiles in magnetite crystals from the fractions 315-500 and 250-315 µm to be carried out with the electron microprobe for Fe-Ti oxides.

## 2.4. Compositional analysis of crystals by EMP

Orthopyroxene crystals have been analysed for major and minor elements (Si, Al, Ca, Mg, Na, K, Ti, Fe, Mn et P) with the electron probe microanalysis (EMP) with an acceleration voltage of 15 kV, a beam current of 10 nA and a focused beam of 2 µm (CAMECA SX-Five and SX-100; Service Camparis, Paris). Calibrations of the EMP were performed with natural mineral samples, which are standards from Service Camparis. The counting times on peak and background for Fe and Mg were set at 80 s and 10 s for the other elements. The core to rim compositional profiles of the zoned orthopyroxene crystals had a 2 µm step and an average length of 100 µm (~4 hours per profile). They were acquired perpendicular to the long axes of the orthopyroxene crystals and away from the corners to avoid three-dimensional

effects such as growth (Allan et al. 2013; Krimer and Costa 2017; Fabbro et al. 2018; Ostorero et al. 2021). Four points were measured in the unzoned orthopyroxene crystals.

For the magnetite profiles, the same analytical conditions as those used for orthopyroxene crystals were used (15 kV, 10 nA and a focused beam of 2 µm) and a counting time of 10 s was set for all the elements except for Fe, Ti and Al (60 s).

## 2.5. Timescales of magmatic processes

Interdiffusion timescales can help to decipher the different pathways of crystals that grew in the plumbing system and highlight changes in magmatic storage conditions (defined as magmatic environments, by changes in temperature, pressure, oxygen fugacity ($fO_2$) and volatile element abundance) (Kahl et al. 2011; Ubide et al. 2019). If the same compositional plateau is found in a significant number of crystals, these plateaus can be inferred to have been produced by significant changes in the magmatic conditions and can be considered as a magmatic environment (Kahl et al. 2011; Ubide et al. 2019). The timescales modelled on these plateau changes allow to constrain the magma dynamics over time.

An En increase in orthopyroxene crystals (reverse zonations) is linked to an increase in temperature, with, or without, mixing of the magma with hotter, more basic magma (Martel et al. 1999; Solaro et al. 2020) or a heating event (Waters and Lange 2017). On the other hand, a decrease in En content (normal zonations) may be related to a decrease in pressure, mixing with cooler magma or degassing (Martel et al. 1999; Saunders et al. 2012; Kahl et al. 2013; Solaro et al. 2020).

### 2.5.1. Fe-Mg interdiffusivity

The main assumption is that the initial profile between the two compositional zones follows a step function. Profiles in which $Al_2O_3$ gradients are decoupled from the Mg number ($\mathrm{Mg\#} = \frac{\mathrm{Mg}}{\mathrm{Mg+Fe_{tot}}}$), are modelled so that the gradients are not due to growth of the crystals but due to interdiffusion of Fe-Mg (Flaherty et al. 2018) (**Supplementary Fig. 5; Supplementary Data 3**). The Fe-Mg interdiffusion profiles were modelled in one dimension, across the c-axis and parallel to the b-axis of the crystals (Allan et al. 2013; Couperthwaite et al. 2020), using the parametrization of the interdiffusion coefficient $D$ of Fe and Mg in orthopyroxene (Ganguly and Tazzoli 1994). $D$ has been defined without an oxygen fugacity $fO_2$ dependence in equation (1) (Ganguly and Tazzoli 1994):

$$\log D = -5.54 + 2.6X_{Fe} - \frac{12530}{T} \quad (1)$$

Tight and realistic constraints on temperature and the diffusion coefficient are the main sources of uncertainty (Morgan et al. 2004; Costa and Morgan 2010; Solaro-Müller 2017; Solaro et al. 2020). Uncertainties in the calibration of measurements and point spacing during EMP analyses, as well as the resolution of SEM images are also sources of uncertainty (Ostorero et al. 2021).

The $fO_2$ dependence on the Fe-Mg interdiffusion coefficient is still under discussion. Ganguly and Tazzoli (1994) did not constrain the $fO_2$ oxygen dependence but they hypothesized that this phenomenon occurred via analogy to the behavior of olivine (exponent of 1/6). The $fO_2$ correction was added in Allan et al. (2013), following this equation (3):

$$\log D = -5.54 + 2.6X_{Fe} - \frac{12530}{T} + \frac{1}{6}\left(\frac{fO_{2,sample}}{fO_{2,IW}}\right) \quad (3)$$

A series of experimental determinations of Fe-Mg interdiffusion in En-rich orthopyroxene crystals ($En_{91}$ and $En_{100}$) constrained a lower $fO_2$ dependence than that inferred from Ganguly and Tazzoli (1994) (with an exponent between 0 and 0.05), but that it depended on the En composition of the crystal (Dohmen et al. 2016). Using their coefficient determined for highly magnesian compositions would then lead to effects of composition on diffusivity, yielding erroneous timescales (Allan et al. 2017). As Allan et al. (2017), we thus used the coefficient of Ganguly and Tazzoli (1994), which includes the compositional range of the orthopyroxene crystals of this study ($En_{59\text{-}68}$; **Supplementary Fig. 8**) and without the oxygen dependence (as it was shown to be weak and not constrained for a wide range of orthopyroxene compositions (Dohmen et al. 2016)).

A new experimental work correlating the experimental Fe-Mg interdiffusion determination in orthopyroxene as a function of Fe content suggests that the use of these calibrations could make timescales about four times longer (Dias and Dohmen 2024). However, the diffusivity is not calibrated at the conditions of interest for magmas, but much hotter (at temperatures between 950 and 1100 °C at constant $fO_2 = 10^{-7}$ Pa) and a factor of 4 is still within the large uncertainties of Ganguly and Tazzoli (1994) so this compositional dependence was not used in this present work.

### 2.5.2. Estimation of temperatures

From glass compositions, thermobarometry of amphibole (Higgins et al. 2022) and looking at microlites and phase assemblages, the temperatures were estimated for a three-level magma storage architecture (Martel et al. accepted). The temperature of the deep reservoir would be ~850 °C, while a shallower reservoir where the magma at the origin of the blast and pumiceous C-PDC resided would be at ~900 °C. The temperature of the subsurface cryptodome would be at ~900 °C from which the laterally directed blast was initiated.

Indeed, considering a maximum glass $SiO_2$ content of 79-80 wt%, quartz crystallizes at maximum temperatures of ~850 °C at 100 MPa and ~925 °C at 50 MPa (Martel et al. 2021), which constrains the conditions of the shallow reservoir (Martel et al. accepted). For the deep reservoir, the range of the calculated temperatures using Higgins et al. (2022) are of ~840-990 ± 6.5-50 °C. This temperature range is a largely realistic estimate within the given uncertainties. The main amphibole population calculated temperature conditions at 850 ± 50 °C (between ~840-865 ± 16 °C). Considering the uncertainties, from amphibole thermobarometry, melt inclusion compositions, the presence of quartz, and the absence of cristobalite, the upper part of the deep reservoir temperature is inferred to have a homogeneous temperature of ~850 °C (Martel et al. accepted).

A minor amphibole population recorded deeper and hotter storage areas: 850-990 °C, likely corresponding to the base of the deep reservoir. In Martel et al. (accepted), the compositions of melt inclusions and their orthopyroxene hosts are also given for the pumiceous C-PDC (d'Augustin 2021) and equilibrium temperatures are estimated here using the orthopyroxene-liquid thermometer (equation 28a) of Putirka (2008), using the compositions of melt inclusions hosted in orthopyroxene crystals (**Supplementary Table 2**). The orthopyroxene-liquid thermometer constrains the diffusion temperature of orthopyroxene crystals, and can allow to determine the closest diffusion temperature for each orthopyroxene rim modelled (Mangler et al. 2022).

| Sample | Thermobarometry in amphibole, melt inclusions, glass compositions, and looking at microlites and phase assemblage Martel et al. (accepted) |
|---|---|
| **Blast** | Deep reservoir: 850 ± 50 °C; shallow storage: 900 ± 50 °C |
| **Post-blast pumiceous C-PDC** | 931 ± 26 °C (equation 28a; Putirka 2008) for C-PDC pumices: 36 orthopyroxene-hosted melt inclusions (Martel et al.in review; d'Augustin 2021; Ostorero 2022)) |

**Supplementary Table 2 Temperatures from Martel et al. (accepted) using amphibole, quartz crystallization temperatures and those estimated using orthopyroxene melt inclusions** from the post-blast pumiceous C-PDC (Putirka 2008) (melt inclusions compositions from Martel et al. (accepted), d'Augustin (2021) and Ostorero (2022)) **(Supplementary Fig. 2)**

As all these temperature estimates overlap considering their uncertainties (**Supplementary Fig. 2**), we considered that the most likely temperatures estimates were from the ones estimated using different constraints: phase compositions, microlite compositions and amphibole thermobarometry (Martel et al. accepted).

Temperatures of 900 ± 50 °C and 850 ± 50 °C, which correspond to the estimated magma temperatures in the shallow reservoir and deep reservoir, respectively (Martel et al. accepted), were used for the diffusion models. We considered that the inner normal zonations in orthopyroxene crystals (from the core to the first compositional band) were formed in the deep reservoir, at a lower temperature (850 °C) than did the other oscillating bands in multiple-zoned crystals (in the shallow reservoir, 900 °C) as it is likely that they crystallized at a lower temperature (see **Results** and **Supplementary Materials**). These timescales correspond to only 6 timescales out of the 92 modelled.

This reasoning was inspired by the diffusion model NIDIS (Petrone et al. 2016, 2018), developed for clinopyroxenes, which considers several temperatures to constrain the crystal lifetime history. It uses a backward approach to deconstruct the zoning profiles of clinopyroxenes, which was not applied to our crystal set because only two temperatures were estimated for the two storage zones and specific temperatures corresponding to each oscillating band of the complexly zoned orthopyroxene crystals were not known. However, corrections of the different temperatures used are shown in **Supplementary Data 6** for the two crystals impacted (one core-inner normal-zoned band modelled at 850 °C and one rim modelled at 900 °C).

### 2.5.3. Timescales modeling method for orthopyroxene crystals

The model used to estimate the timescales for orthopyroxene with the Fe-Mg diffusion coefficient of Ganguly and Tazzoli (1994) is the AUTODIFF spreadsheet adapted for orthopyroxene (Allan et al. 2013; Hartley et al. 2016; Pankhurst et al. 2018; Couperthwaite et al. 2020; Ostorero et al. 2021, 2022). A demo version of AUTODIFF_opx can be found in **Supplementary Data 1** (**Supplementary Fig. 3**).

It consists in the intercalibration of chemical composition profiles of zoned orthopyroxene crystals measured with an electron microprobe, with grayscale profiles on high-resolution north-south oriented images taken with SEM (magnification of 75 and spatial resolution of 0.14 µm) (**Supplementary Fig. 3**). The Mg number is the parameter that seems to best control the grayscale of the images (Morgan et al. 2004; Petrone et al. 2016; Solaro-Müller 2017; Couperthwaite et al. 2020). *ImageJ* software (https://imagej.nih.gov/ij/; version 1.52a) was used to produce grayscale profiles, which were averaged over a certain width to reduce the noise (between 20 to 50 µm, depending on the crystal rim size) (Solaro et al. 2020; Ostorero et al. 2021). After this intercalibration, the profiles are modelled to obtain the timescales of interdiffusion. Based on a database of contrasts of particular compositions calculated using a finite difference method, the curve that best fits the curve obtained by intercalibration was searched in this database (Couperthwaite et al. 2020). After rescaling the two curves, the timescale corresponding to the zonation is obtained, as the scaling factor depends on the ratio between the timescales of the database and the time associated with zoning in the crystal (Solaro et al. 2020).
The main assumption of the model is that the initial profile between two zones follows a step function, which is modified by diffusion to form sigmoidal concentration gradients and, with time, this steep profile becomes broader, due to interdiffusion of the different elements. During the eruption, the profiles are quenched due to a major decrease in temperature. The maximum timescales are then estimated (Morgan et al. 2004).

Regarding the total residence timescales, if the temperatures of formation of each band are known, it is possible to determine the total residence timescales of a crystal. This model is the Non-Isothermal Diffusion Incremental Step model (NIDIS), which allows to deconstruct multiple-zoning profiles in different isothermal steps with their own diffusion coefficients (Petrone et al. 2016, 2018). If an internal band grows at a temperature $T_1$ during a time $t_1$ ($\Delta t_1$) and elements diffuse with a diffusion coefficient $D_1$ at $T_1$, and then if a second band grows at a different temperature $T_2$, and diffuses until the time of the eruption $t_2$ ($\Delta t_2$) with a $D_2$, it will affect the whole crystal and the elements in the first band will also diffuse with the new diffusion coefficient $D_2$. The shape of the first band changes as the temperature has changed. The sigmoid curves of the diffusion profile thus evolve during the whole thermal history of the pyroxene. The NIDIS model uses a backward approach because the diffusion coefficient has changed during the history of the crystal and to retrieve the real time that the first band took to diffuse $\Delta t_1$.
However, in this study, as the temperatures associated with each zoning band and compositional changes were not known here, the same temperature was used for all external rims (900 °C; and a lower temperature of 850 °C was used for normal core-inner bands) (Martel et al. accepted). The NIDIS model was thus not used because the zoning patterns of the orthopyroxene crystals were too complex.
A Monte-Carlo simulation was used to estimate the integrated time uncertainty from the different sources of uncertainty (on $T$, $D_0$, $Ea$ and resolution of grayscales values of SEM images), giving asymmetric uncertainties, with a larger error bar on the positive error and a smaller error bar on the negative error.

### 2.5.4. Timescales modeling method for magnetite crystals

Fe-Ti oxides, and magnetite crystals in particular, are known to rapidly re-equilibrate (within a few days to months) in response to fluctuations in magmatic conditions such as temperature, surrounding fluid

composition or oxygen fugacity $fO_2$ influencing the partitioning of elements at equilibrium (Freer and Hauptman 1978; Aragon et al. 1984; Nakamura 1995; Venezky and Rutherford 1999; Martel et al. 1999; Devine et al. 2003; Coombs and Gardner 2004; Allan et al. 2017; Sievwright et al. 2020).

If crystals of magnetite are unexsolved, their Ti content may be used to constrain $T$ and/or $fO_2$ changes during late stages of magma ascent in the conduit and magnetite crystallization, shortly before quenching (timescales of the order of days to months) (Nakamura 1995; Boudon et al. 2015).

Ti diffusion magnetite was characterized by using the diffusion relationship constrained by Aragon et al. (1984), described in equation (2):

$$D_{Ti}^{*} = D_0^0 e^{-\left(\frac{E_0}{RT}\right)} + D_V^0 e^{-\left(\frac{E_v}{RT}\right)} f_{O_2}^{2/3} - D_I^0 e^{-\left(\frac{E_I}{RT}\right)} f_{O_2}^{-2/3} \quad (2)$$

For $T$ of interest and $fO_2$ of interest, where $D_0^0 = 8.2 \times 10^{-3}$ cm$^2$/s ; $D_v^0 = 1.75 \times 10^{-12}$ cm$^2$ (s atm$^{2/3}$); $D_I^0 = 3.9 \times 10^6$ (cm$^2$ atm $^{2/3}$)/s; $E_0 = 60$ kcal/mol; $E_v = -28$ kcal/mol, and $E_I = 159$ kcal/mol.
Ti profiles of unexsolved magnetite crystals were obtained using first SEM images of magnetite crystals hand-picked in the 315-500 and 250-315 µm fractions to identify the best profiles for diffusion modeling. Ti profiles are not visible in the SEM images by variations of greyscale intensities as in zoned orthopyroxene crystals (with a low contrast in composition). However, the occurrence of a ring of melt inclusions in magnetite crystals has been shown to be an indicator of zonations, by a previous study on magnetites in lava dome clasts (Boudon et al. 2015) (**Supplementary Fig. 3**). Then, quantitative Ti profiles were analyzed after the EMP sessions. Diffusion profiles are between 100 and 180 µm long, from core to rim with a 2 µm step.

Ti diffusion profiles for zoned magnetite crystals were fit using the same temperatures as those for orthopyroxene crystals (the ones estimated by Martel et al. (accepted)), and the oxygen fugacity of ~1.5 above NNO was used (**Supplementary Table 2**; **Supplementary Fig. 2-3**) (Martel et al. accepted). The initial conditions are a step function, using the AUTODIFF_mgt spreadsheet with a diffusion model, using the same method as in Boudon et al. (2015). A demo version of AUTODIFF_mgt can be found in **Supplementary Data 2** (**Supplementary Fig. 3**). The uncertainty is estimated by propagating the temperature uncertainties onto the timescale.

### 2.5.5. Timescales from multiple-zoned orthopyroxene crystals

Timescales in multiple-zoned crystals have been modelled in several of their internal bands or external rims when possible. The bands were modelled independently, as AUTODIFF is not handling multiple-zoned profiles (not handling multi-steps) and as the diffusion timescales were not always modelled on successive bands (e.g. timescales modelled from B1 to B2 and B3 to B4 but not on B2 to B3). The following **Supplementary Table 4** shows the total timescales considering the modelled bands in the same crystal. For the bulk of the modelling, it is done at 900°C. In cases where a core and rim are both modelled at the same temperature, time elapsed in the time period where the rim was diffusing is equivalent to and diffusing at the same speed as the time elapsed in the core, so there is no differential diffusion. Correcting for different zone residence only arise where the core and rim diffusion have been modelled at different temperatures. In our samples, it corresponds to the crystals where a core run at 850°C and a rim at 900°C. This can be corrected using an offline calculation, and it only applies to two crystals in our entire dataset (whilst there are several normal inner bands modelled at 850°C, not all of them also have rim zones modelled at 900°C). **Supplementary Table 4** shows the total timescales considering the modelled bands in the same crystal, while a tab in **Supplementary Data 6** shows the timescales correction of the two crystals (one in the blast and one in the pumiceous C-PDC) where inner normal bands where modelled at 850°C and rims at 900°C.

Considering the uncertainty associated to the oldest timescale modelled, the total timescale is always overlapping with the positive error of the oldest timescale modelled for each multiple-zoned orthopyroxene. So, as in most cases, not all the compositional bands of the orthopyroxene were modelled in time, the individual timescales are discussed in the main text rather than the total timescales, as some timely information are missing from them with the other compositional bands not modelled in time.

| **Sample** | **Crystal** | **Sequence of bands** | **Oldest timescale modelled (days)** | **Total timescale (days)** | **Total timescale (years)** |
|---|---|---|---|---|---|
| Blast | Bezy8f_315_L8C22 | B2-B3 + B3-B4 | 38 +76/-25 | 75 | 0.2 |
| Blast | Bezy8f_315_L5C16 | B5-B6 + B6-B7 | 55 +112/-37 | 99 | 0.3 |
| Blast | Bezy3e_250_L3C3 | B2-B3 + B3-B4 | 102 +210/-68 | 124 | 0.3 |
| Blast | Bezy8f_250_L7C27 | B1-B2 + B2-B3 | 95 +212/-66 | 137 | 0.4 |
| Blast | Bezy8f_250_L6C3 | Core-B1 + B1-B2 | 128 +303/-90 | 107 (see **Supplementary Data 6** for explanations) | 0.3 |
| Blast | Bezy3e_315_L3C15 | B5-B6 + B6-B7 | 132 +279/-90 | 140 | 0.4 |
| Blast | Bezy3e_315_L3C16 | B4-B5 + B5-B6 | 120 +256/-81 | 146 | 0.4 |
| Blast | Bezy3e_315_L3C20 | B5-B6 + B6-B7 | 251 +512/-168 | 274 | 0.7 |
| Blast | Bezy3e_315_L4C27 | B4-B5 + B7-B8 | 176 +368/-119 | 284 | 0.8 |
| Blast | Bezy8f_250_L7C15 | B4-B5 + B5-B6 | 322 +3307/-293 | 480 | 1.3 |
| Blast | Bezy8f_315_L5C1 | B6-B7 + B7-B8 | 472 +998/-321 | 655 | 1.8 |

| | | | | | |
|---|---|---|---|---|---|
| Blast | Bezy3e_315_L1C2 | B3-B4 + B4-B5 | 635 +1323/-429 | 754 | 2.1 |
| Blast | Bezy8f_250_L9C10 | B2-B3 + B3-B4 + B4-B5 | 343 +746/-235 | 789 | 2.2 |
| Blast | Bezy3e_315_L3C22 | B2-B3 + B7-B8 | 668 +1382/-450 | 976 | 2.7 |
| Blast | Bezy3e_315_L4C21 | B6-B7 + B7-B8 | 1951 +4140/-1326 | 1970 | 5.4 |
| | | | | | |
| C-PDC | Bezy9_315_L8C5 | B3-B4 | 98 +200/-66 | 132 | 0.4 |
| C-PDC | Bezy9_125_L2C16d | Core-B1 + B1-B2 | 128 +263/-86 | 133 | 0.4 |
| C-PDC | Bezy9_315_L8C23 | B1-B2 + B3-B4 | 157 +321/-105 | 178 | 0.5 |
| C-PDC | Bezy9_250_L5C29d | B1-B2 + B2-B3 | 302 +977/-231 | 327 | 0.9 |
| C-PDC | Bezy9_125_L5C41g | B1-B2 + B2-B3 | 353 +3102/-317 | 391 | 1.1 |
| C-PDC | Bezy9_315_L5C2 | B1-B2 + B2-B3 | 355 +746/-240 | 574 | 1.6 |
| C-PDC | Bezy9_315_L3C23 | B1-B2 + B2-B3 | 518 +1098/-352 | 659 | 1.8 |
| C-PDC | Bezy9_315_L4C25 | B2-B3 + B4-B5 | 551 +1192/-377 | 671 | 1.8 |
| C-PDC | Bezy9_315_L6C10 | Core-B1 + B1-B2 + B2-B3 | 1058 +2325/-727 | 1711 | 4.7 |
| C-PDC | Bezy9_315_L4C13 | B1-B2 + B2-B3 + B3-B4 | 1265 +2773/-869 | 2142 | 5.9 |
| C-PDC | Bezy9_315_L2C15 | Core-B1 + B1-B2 | 1367 +3362/-972 | 2197 | 6 |
| C-PDC | Bezy9_250_L8C7g | Core-B1 + B1-B2 | 4483 + 36587/-3137 | 4479 (see **Supplementary Data 6** for explanations) | 12.3 |

**Supplementary Table 3 Total timescales adding up the diffusion timescales modelled on the different bands in multiple-zoned orthopyroxene crystals from the blast or from the C-PDC pumices (Supplementary Data 6).**

### 2.5.6. Timescales from amphibole

Amphibole crystals were first identified in overview BSE image maps of the rock mounts, and then imaged in detail at magnifications of ~100 to 1000 for five to 20 crystals per sample. The thickness of amphibole decomposition rims was then measured using these high-resolution BSE images. Amphibole crystals that were cut approximately parallel to one of their main crystallographic axes were selected for the measurement. Rim thicknesses were measured in 10-20 µm increments along the rims and averaged, excluding sections close to crystal corners or irregularities. As in other studies, we estimated a measurement uncertainty of ~ ± 2 µm (Rutherford and Hill 1993). With this approach, we were able to quantify the minimum amphibole rim thicknesses for the samples, but could not detect or quantify the presence of amphibole with rims of variable thickness within single samples, i.e. crystals that have been assembled over a range of timescales (for which 3D techniques would have to be applied). Experimentally constrained rates of amphibole decomposition at 4 to 90 MPa and 840 to 900 °C (Rutherford and Hill 1993; Rutherford and Devine 2003; Browne and Gardner 2006), which are conditions in the range of those inferred for shallow and very shallow intermittent magma storage (Martel et al. accepted), were then used to constrain the minimum residence times of magma parcels within the shallowest part of the system at <100 MPa. We highlight here, and later discuss, that we consider the single-step decompression experiments of Rutherford and Hill (1993) and Browne and Gardner (2006) as most applicable for constraining amphibole decomposition times for Bezymianny 1956 eruption products, because they formed during intermittent magma storage at low and very low pressures (Martel et al. accepted) and not during continuous ascent as characterized in multi-step decompression experiments. Timescales from amphibole rim thicknesses are reported in **Supplementary Table 4**.

| Eruption type | Sample name | Lithology | Amphibole rim type | Amphibole rim thickness (µm) | Broad estimate (days) | Best estimate (days) |
|---|---|---|---|---|---|---|
| Blast | Bezy3e | Vesiculated clast | Intermediate type (1 to 2) | 9 ± 2 | 1.5 ± 0.3 - 18 ± 3.8 | 5 ± 1.0 – 18 ± 3.8 |
| | Bezy7a-66 | Dense clast | 2 | 24 ± 3 | 4.0 ± 0.6 - 48 ± 6.8 | > 16 ± 2.3 – 48 ± 6.8 |
| | Bezy7a-67 | Vesiculated clast | Intermediate type | 12 ± 2 | 2.0 ± 0.4 – 24 ± 4.4 | 6 ± 1.1 – 24 ± 4.4 |
| | Bezy7a-70 | Highly vesiculated clast | 1 | 9 ± 2 | 1.5 ± 0.3 - 18 ± 3.8 | 1.5 ± 0.3 – 7 ± 1.5 |
| | Bezy7a-84 | Dense clast | 2 | 29 ± 4 | 4.8 ± 0.7 – 58 ± 7.8 | > 19 ± 2.6 – 58 ± 7.8 |
| | Bezy7a-86 | Dense clast | 2 | 22 ± 3 | 3.7 ± 0.5 – 44 ± 6.4 | > 15 ± 2.1 – 44 ± 6.4 |
| | Bezy7b-8 | Pumice | 1 | 10 ± 2 | 1.7 ± 0.3 - 20 ± 4.0 | 1.7 ± 0.3 – 8 ± 1.5 |
| | Bezy7b-13 | Vesiculated clast | Intermediate type | 16 ± 3 | 2.7 ± 0.4 – 32 ± 5.2 | 8 ± 1.3 - 32 ± 5.2 |

| | | | | | | |
|---|---|---|---|---|---|---|
| | Bezy8b | Dense clast | 2 | 27 ± 4 | 4.5 ± 0.6 – 54 ± 7.4 | >18 ± 2.5 – 54 ± 7.4 |
| **Post-blast C-PDC pumices** | Bezy9-17 | Pumice | 1 | 6 ± 2 | 1.0 ± 0.3 - 12 ± 3.2 | 1.0 ± 0.3 - 5 ± 1.2 |
| | Bezy9-107 | Pumice | 1 | 11 ± 2 | 1.8 ± 0.4 – 22 ± 4.2 | 1.8 ± 0.4 – 8 ± 1.6 |

**Supplementary Table 4 Amphibole characteristics of the blast and pumiceous C-PDC. The rim types, rim thicknesses and timescale estimates (days) are shown using the whole range of rim growth rates inferred from Rutherford & Hill (1993) and Browne & Gardner (2006) and the inferred likely rim growth rates from Fig. 9. The uncertainties on the rim thicknesses are on the same order of magnitude as those of Rutherford & Hill (1993) (~ 2 µm for a 10 µm thick rim and ~ 5 µm for a 40 µm thick rim)**

## 3. Supplementary Figures

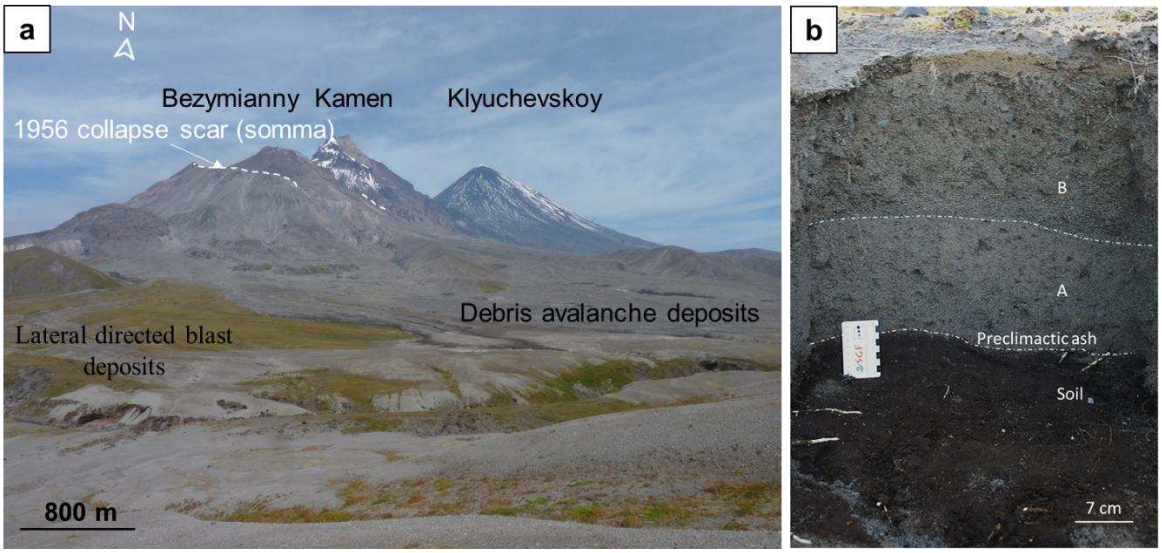


**Supplementary Fig. 1 Bezymianny volcano and its closest neighboring volcanoes (taken in August 2019 by L. Ostorero) (a) and example of a sampling site of the laterally directed blast deposits of the 1956 Bezymianny eruption (b). On (a), the white dashed line shows the collapse scar of the Bezymianny collapse in 1956, and deposits of debris avalanche and directed blast from 1956 are located below the new deposits from the eruptions that followed and their approximate locations are shown on the picture. In (b), two layers are visible in the photo, called layers "A" and "B" (according to the study of Belousov (1996)). Layer A is poorly sorted, enriched in dense juvenile andesitic clasts and contains a mixture of soil and uncharred plant remnants, whereas layer B is well-sorted, with graded beddings, mainly normal grading, and contains rare carbonized plants (Belousov 1996). Layer C overlies layer B (Belousov 1996), but is not visible here. This layer is characterized by intermediate sorting and enrichment of more vesiculated juvenile andesitic clasts, a large percentage of fine fraction and very rare vegetation (Belousov 1996). These layers have different lithologies, sorting and grading that result from rapid evolution of the sedimentation regimes of the diluted and turbulent pyroclastic density currents of the blast (Belousov and Belousova 1998)**

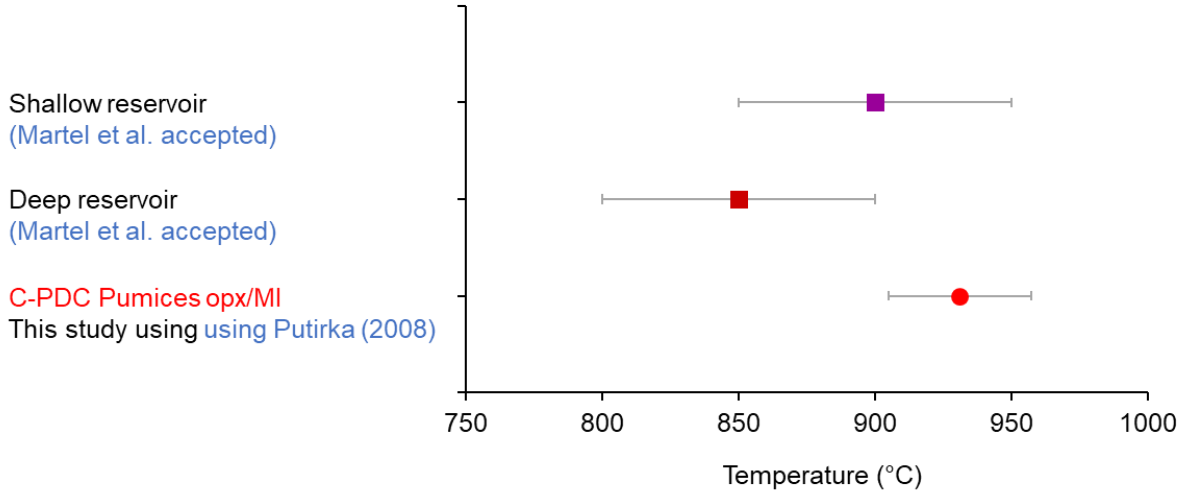


**Supplementary Fig. 2 Summary of the temperatures estimated for the blast and C-PDC pumices of 1956 eruption of Bezymianny (Supplementary Table 2). Martel et al. (accepted) used several constraints: amphibole thermobarometry (Higgins et al. 2022), microlite and phase compositions. Error bars correspond to the standard deviations of each average temperature. All the error bars practically overlap and the temperatures estimated for the shallow and deep reservoir consider all the temperature ranges determined with other methods so these temperatures are kept for the modelling of the timescales in orthopyroxene and magnetite crystals.**

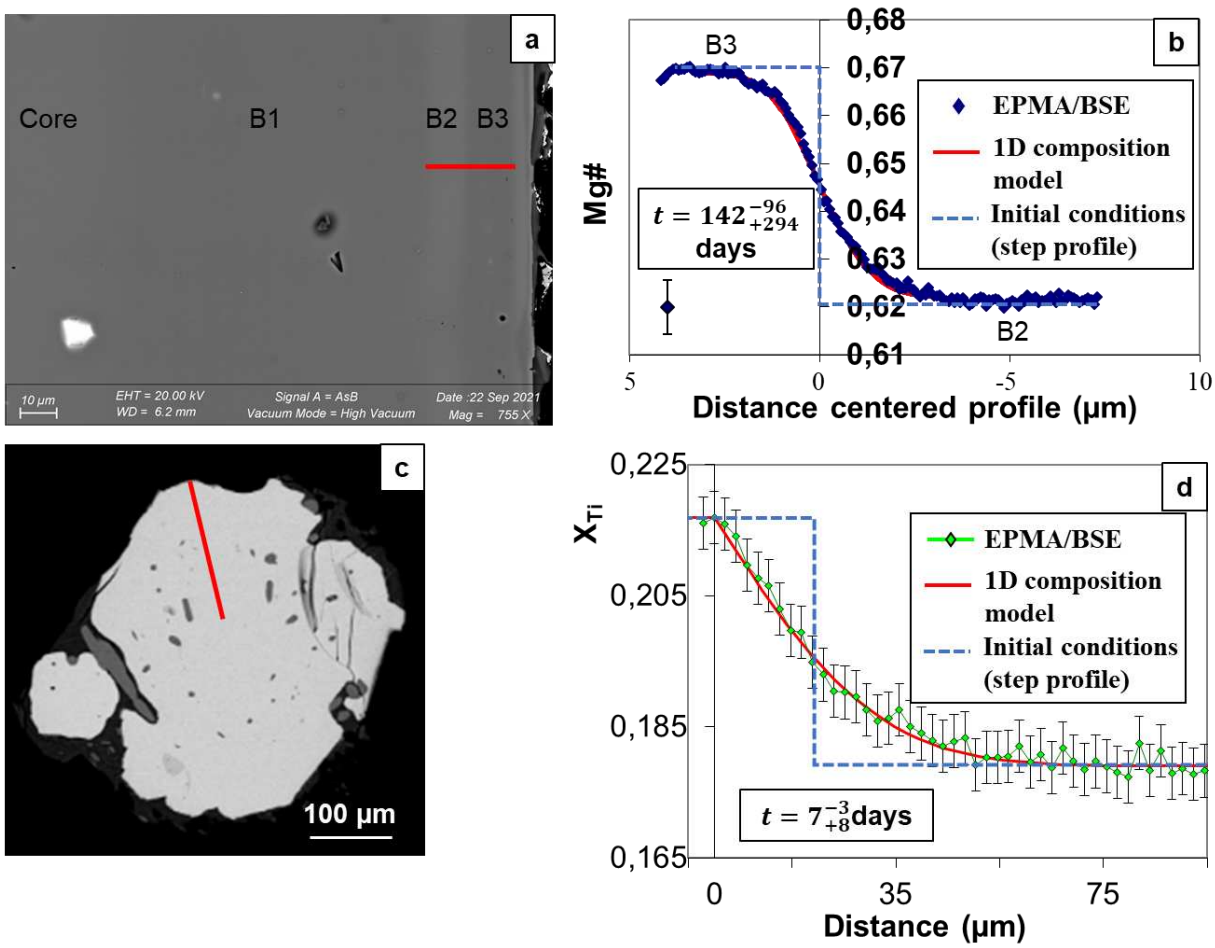


**Supplementary Fig. 3 BSE images of a multiple-zoned orthopyroxene (a) and magnetite (c) and their best-fit models (b and d). b) 1D model and best-fit profile obtained after intercalibration of EMP data of the multiple-zoned orthopyroxene ("B" for bands) and the gray level profile for a temperature of 900 °C. D: diffusivity of Ganguly and Tazzoli (1994). (c-d) Magnetite showing a ring of melt inclusions indicating the presence of a Ti chemical gradient and (d) $X_{Ti}$ profile as a function of distance from the rim (µm), in green and in blue, the Ti diffusion model using the D expression of Aragon et al. (1984).**

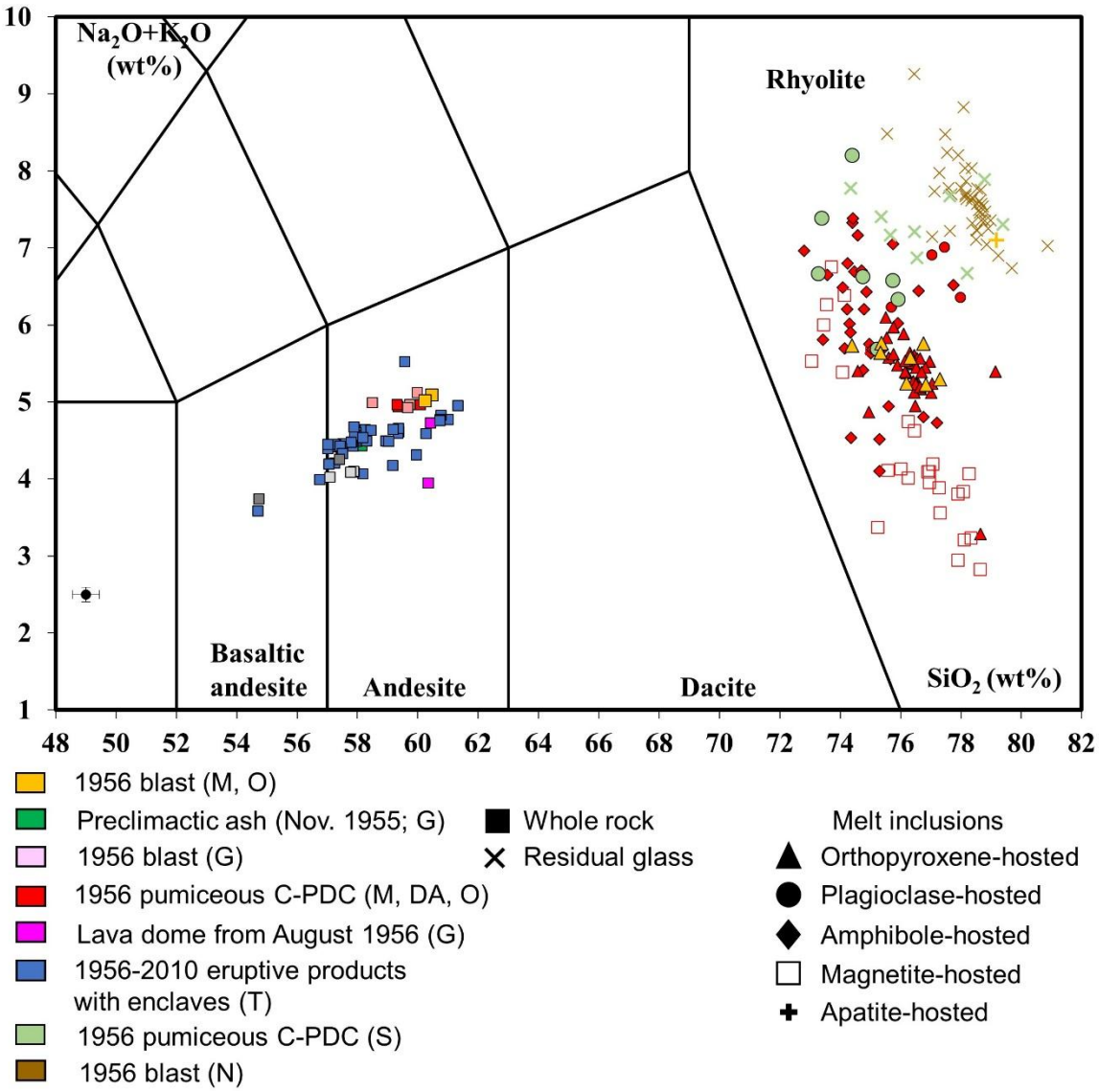


**Supplementary Fig. 4 Total Alkali Silica (TAS) diagram of Bezymianny. Compositions are shown for whole rocks, melt inclusions and residual glasses for the 1956 blast and pumiceous C-PDC. Whole rocks compositions and melt inclusions of the pumiceous C-PDC are from d'Augustin (2021) (noted as "DA"), while whole rocks and melt inclusions for the blast are from Ostorero (2022) (noted as "O"). One melt inclusion in apatite was measured in the pumiceous C-PDC by Martel et al. (accepted) ("M"). The data for Bezymianny are shown from 1956 to 2010 with whole rocks of eruptive products with enclaves (Turner et al. 2013) ("T"). The compositions of the preclimactic ashes (Vulcanian-type ash eruptions) are specified (collected 12 km away from the volcano on 7 November 1955, with orthopyroxene crystals, plagioclase crystals and small inclusions of magnetite), as well as blast deposits from the 1956 climactic phase (different lavas than the preclimactic phase, more acid amphibole andesites) and a lava dome fragment from the new dome that grew directly after the lateral blast (up to August 1956 where the growth was complete) (Gorshkov 1959) ("G"). Residual glasses in the pumiceous C-PDC and melt inclusions in plagioclase were measured by Shcherbakov et al. (2013) ("S") and residual glasses from the blast by Neill et al. (2010) ("N") are also shown**

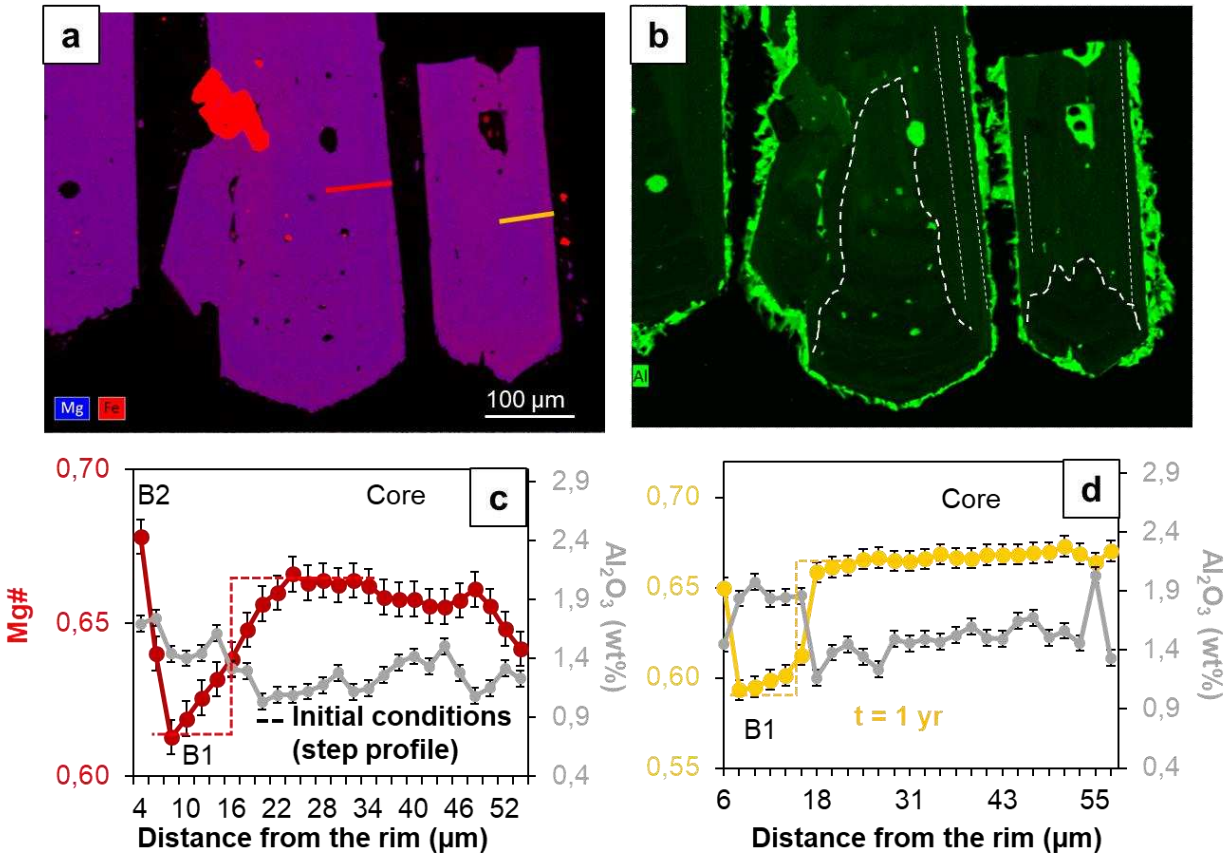


**Supplementary Fig. 5 Compositional maps of Mg and Fe (a) and Al (b) for a multiple-zoned and normal-zoned orthopyroxene, respectively. The Al map shows evidence for sector zoning, indicating rapid growth (Flaherty et al. 2018). (c-d) Profiles of Mg# and $Al_2O_3$ contents (wt%) of the orthopyroxene in (a-b); the profiles locations are shown in (a), with red and orange curves, respectively. They show decoupling of Mg# and $Al_2O_3$ and higher frequency variations in Al than Mg# (such as in Flaherty et al. (2018)), showing that these gradients in Mg# are due to diffusion and not growth**

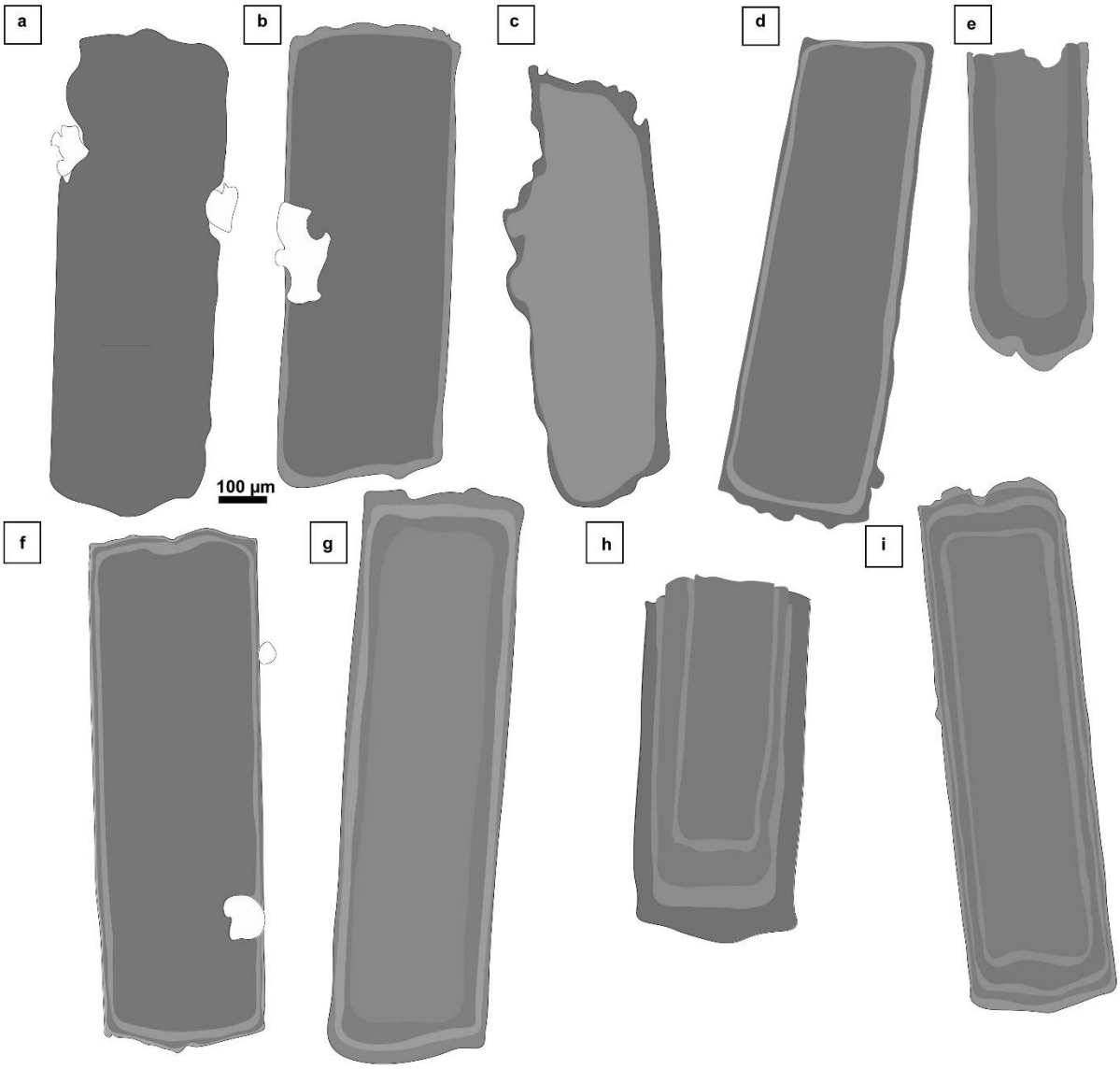


**Supplementary Fig. 6 Schemes of the zoning patterns corresponding to Fig. 3. (a) Unzoned orthopyroxene; b-c) Single-zoned orthopyroxene: normal-zoned (b); and reverse-zoned (c); (d-i) Multiple-zoned orthopyroxene, either normal + reverse (d) or reverse + normal (e) or with three bands: normal + reverse + normal (f) or reverse + normal + reverse (g) or with 4 bands (h) or more than 5 bands (i). The scale is the same in all images as in (a)**

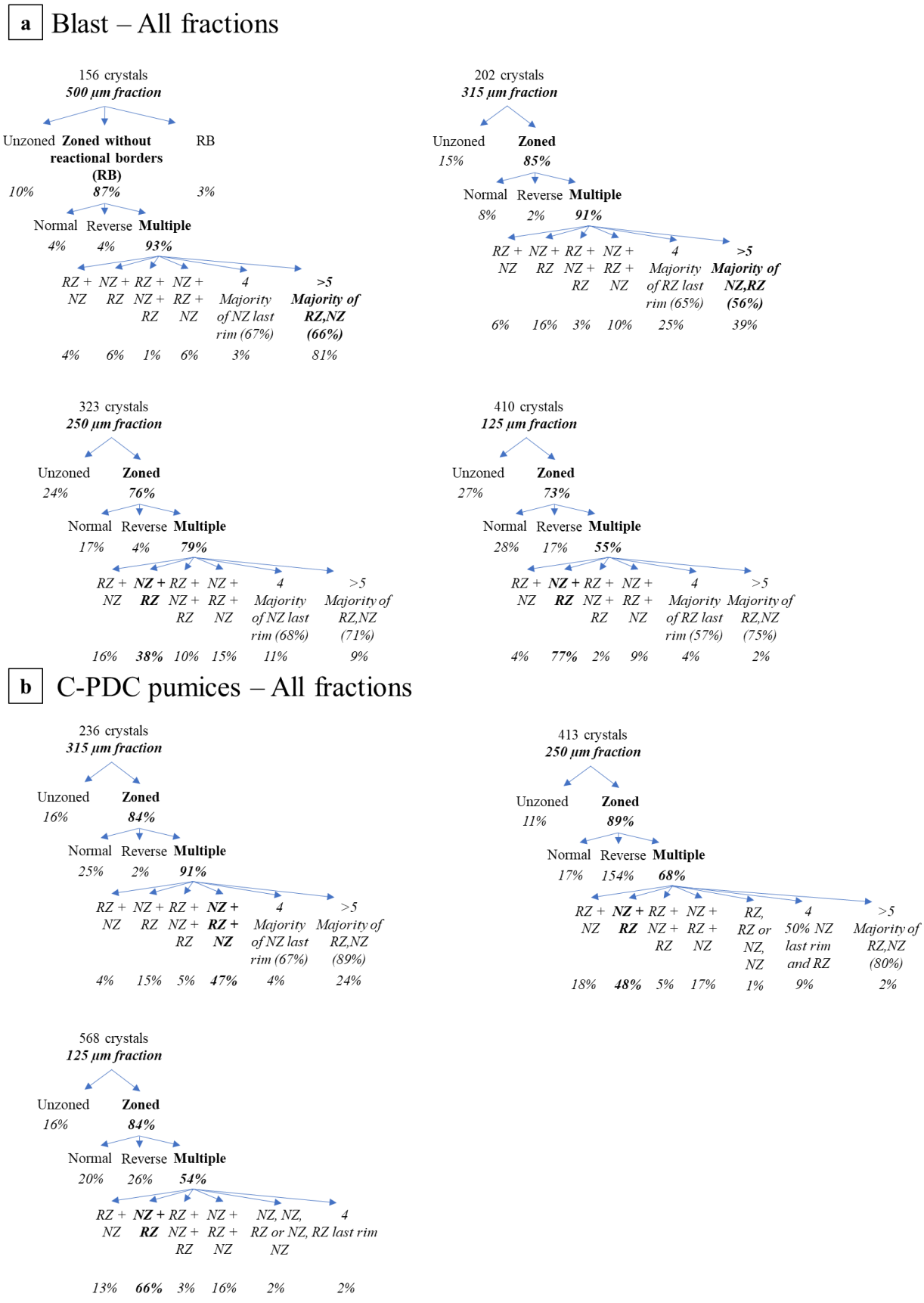


**Supplementary Fig. 7 Proportions of the zonations identified in the orthopyroxene crystals of the blast in each fraction (500-710, 315-500, 250-355 and 125-250 µm) (a) and in the pumiceous C-PDC of the 1956 eruption of Bezymianny in the fractions 315-500, 250-355 and 125-250 µm (b).**

**Single-zoned orthopyroxene crystals: SZ, with normal-zoned (NZ) or reverse-zoned orthopyroxene crystals (RZ), multiple-zoned orthopyroxene crystals (MZ), either reverse + normal (RZ + NZ) or normal + reverse (NZ + RZ), with a third band or 4 (where the nature of the external rim is specified, even MZ with 5 zonations or more are found (nature of the two last bands specified). For the blast, the two highest size fractions have a majority of multiple-zoned orthopyroxene crystals with more than five bands (39-81 %) (Supplementary Fig. 6). For the pumiceous C-PDC, the majority of the multiple-zoned orthopyroxene crystals show three bands (for the higher size fraction: first, a normal-zoned rim; second, reverse zoning; and last, normal-zoned rims; 47 %; Supplementary Fig. 6) or normal- and reverse-zoned rims (the two lowest size fractions; 48-66 %; Supplementary Fig. 6).**

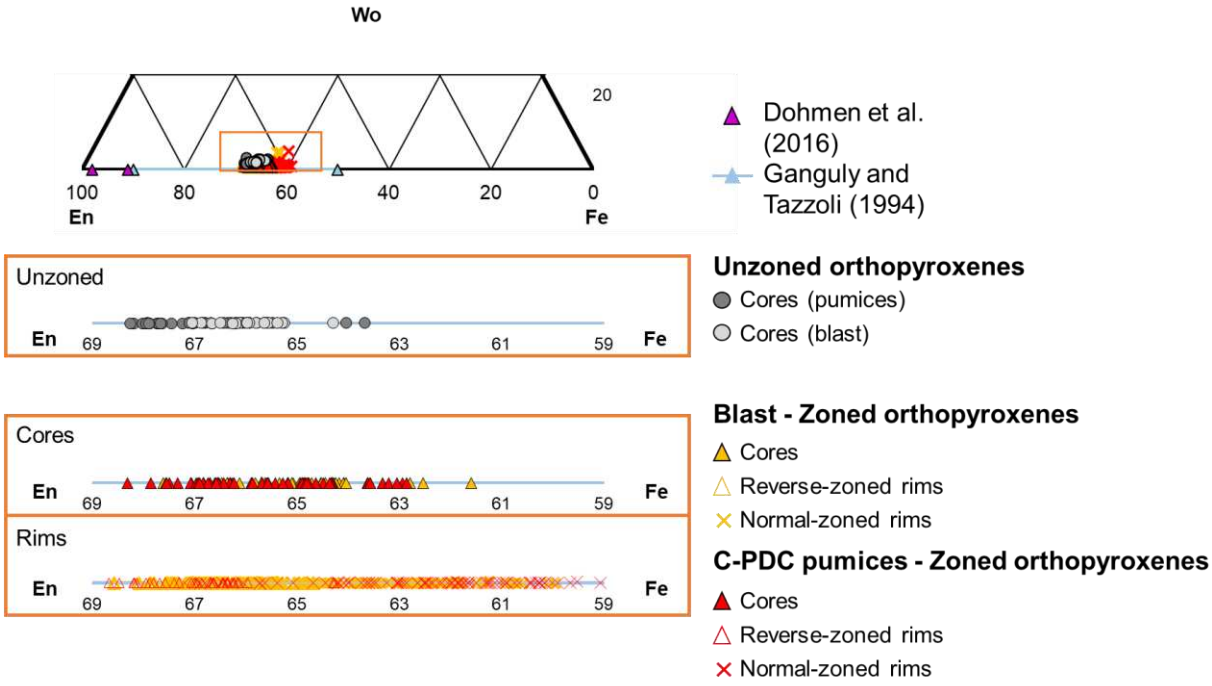


**Supplementary Fig. 8 Ternary diagram of the unzoned and zoned orthopyroxene crystals compositions of the blast clasts and C-PDC pumices from Bezymianny 1956 eruption, with a focus on the Enstatite (En) and Ferrosilite (Fs) poles (Wollastonite (Wo) being the last pole). Orange squares: close-ups of the orthopyroxene's compositions of this study. In blue: the En content range for which the Fe-Mg interdiffusion coefficient parametrization is formulated (Ganguly and Tazzoli 1994) compared to the compositions of the Fe-Mg interdiffusion coefficient parametrization of another study (Dohmen et al. 2016)**

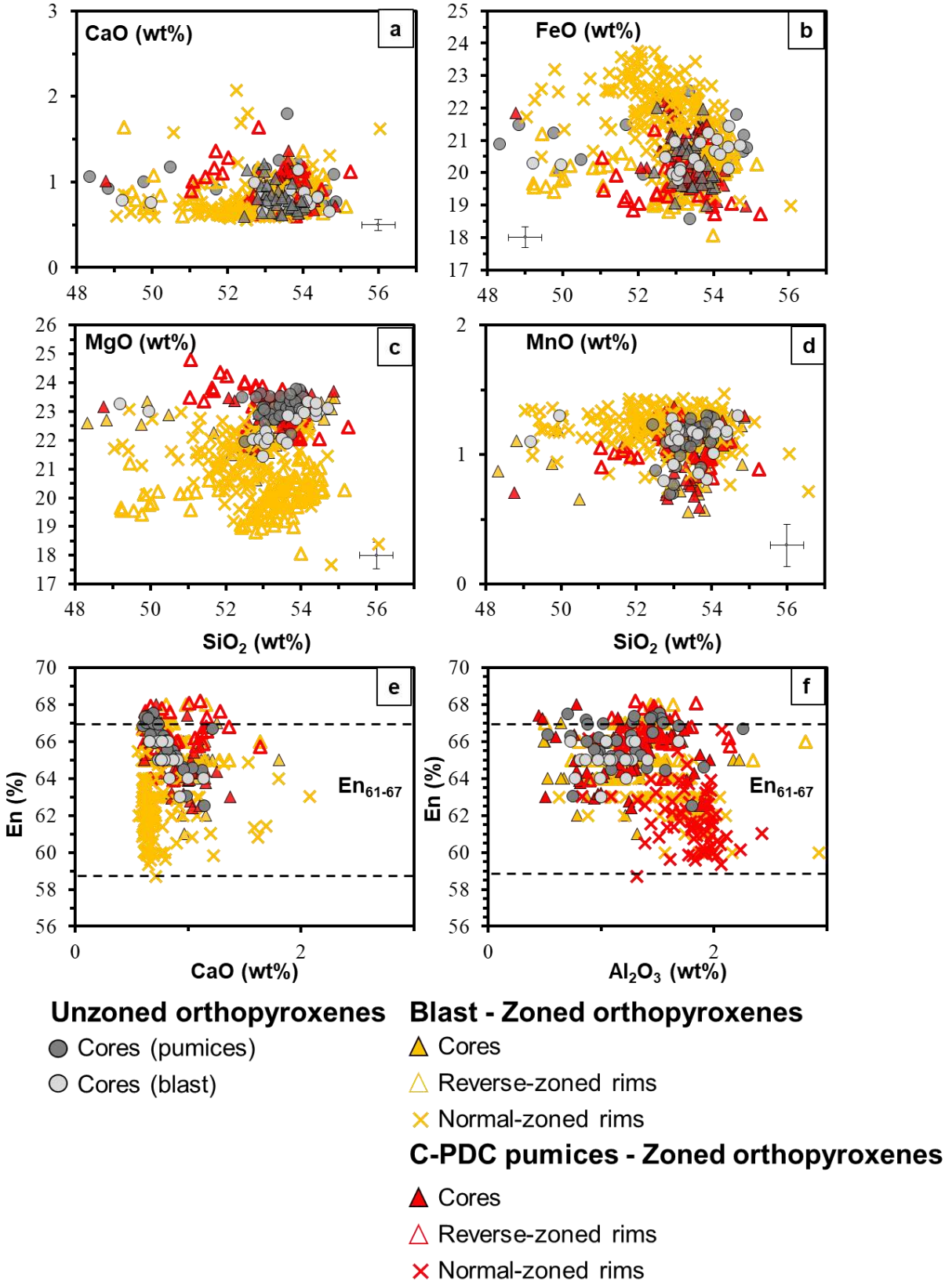


**Supplementary Fig. 9 Composition of the unzoned orthopyroxene crystals compared to the zoned orthopyroxene crystals (reverse and normal rims and their cores) in the blast clasts and C-PDC pumices. a) CaO vs $SiO_2$, b) FeO vs $SiO_2$, c) MgO vs $SiO_2$ and d) MnO vs $SiO_2$, e) En content (%) vs CaO and f) En content (%) vs $Al_2O_3$ (wt%). On all the diagrams, the compositions of the**

**unzoned orthopyroxene crystals and cores of zoned orthopyroxene crystals overlap; $En_{61-67}$ in (e) and (f) and a few rims are outside of these ranges. NZ: normal-zoned; RZ: reverse-zoned**

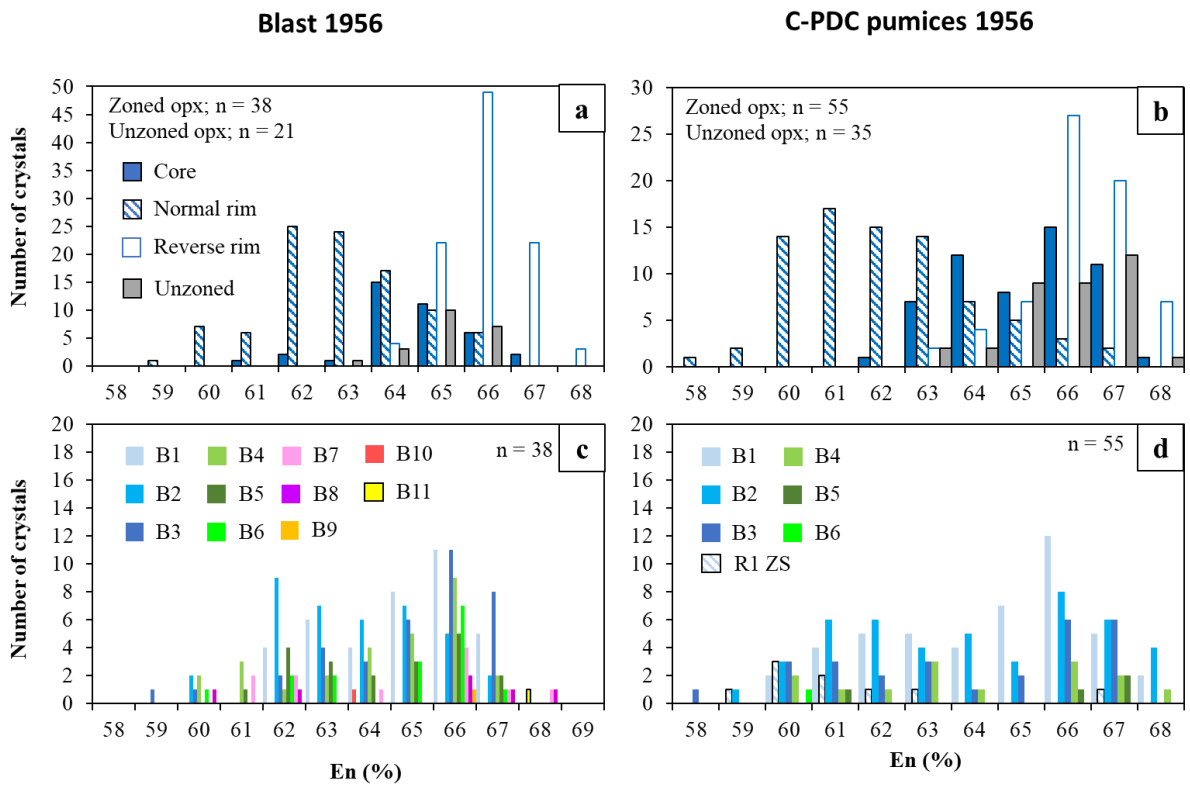


**Supplementary Fig. 10 En contents (%) of the zoned and unzoned orthopyroxene crystals (opx) of the blast and pumiceous C-PDC. a-b) En content of the normal-zoned or reverse-zoned rims of zoned orthopyroxene and unzoned orthopyroxene crystals of the blast and pumiceous C-PDC, respectively. c-d) En content of all the bands ("B") of zoned orthopyroxene crystals of the blast and pumiceous C-PDC, respectively. n is the number of crystals analyzed ("opx" for orthopyroxene)**

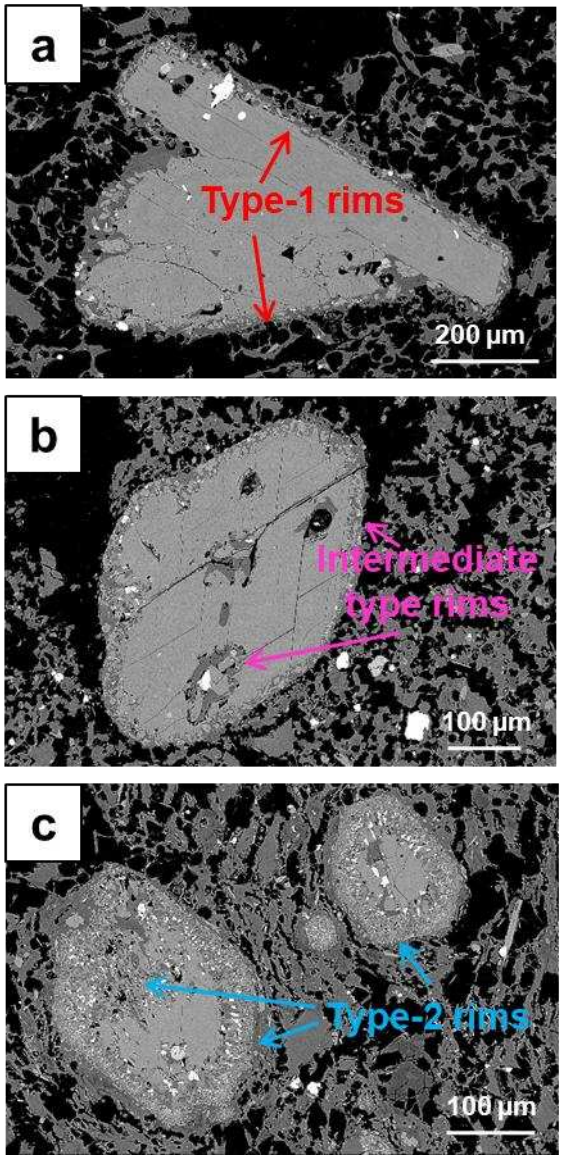


**Supplementary Fig. 11 Amphibole crystals with a range of decomposition rim types in the products of Bezymianny 1956 eruption. (a) Relatively thin, glass-rich, and homogeneous Type-1 decomposition rims, which are characteristic for vesiculated samples of the blast and C-PDC pumices. They occur together with quartz microlites. (b) Moderately thin and glass-rich, relatively homogeneous yet more transgressive intermediate type decomposition rims, which are characteristic for vesiculated clasts of the blast. They occur together with quartz microlites and small cristobalite blebs. (c) Relatively thick, glass-poor, heterogeneous and transgressive Type-2 decomposition rims, which are characteristic of dense clasts of the blast. They occur together with large cristobalite blebs**

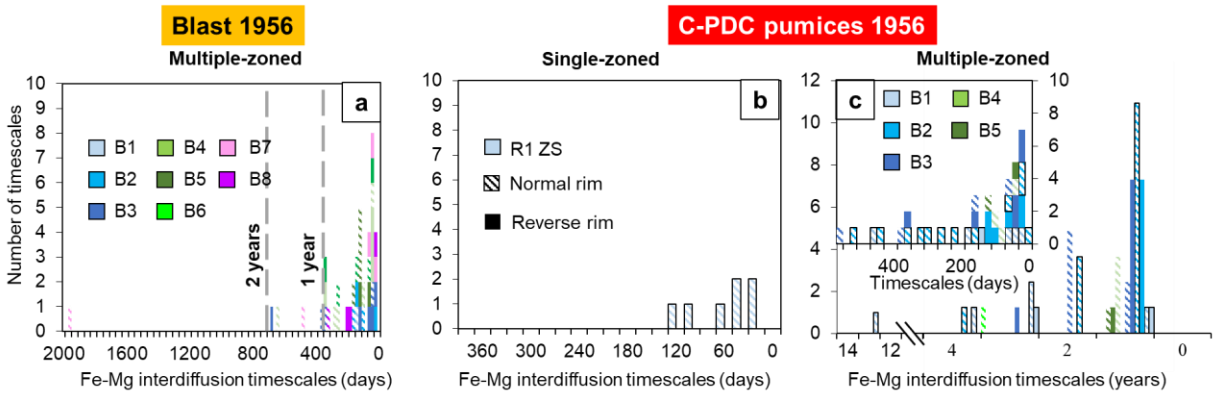


**Supplementary Fig. 12 Histograms of Fe-Mg interdiffusion timescales modelled in orthopyroxene crystals of the blast deposits (a) and pumiceous C-PDC (b-c) at 900 ± 50 °C for core-rim of single-zoned (SZ) and inner-outer bands ("B") of multiple-zoned (MZ) and 850 ± 50 °C for the most inner normal bands of the MZ (core to first inner band), using the temperatures estimated in Martel et al. (accepted). The type of zonation is specified (reverse-zoned or normal-zoned). The timescales are presented as times before the eruptions and can be found in Supplementary Data 5.**

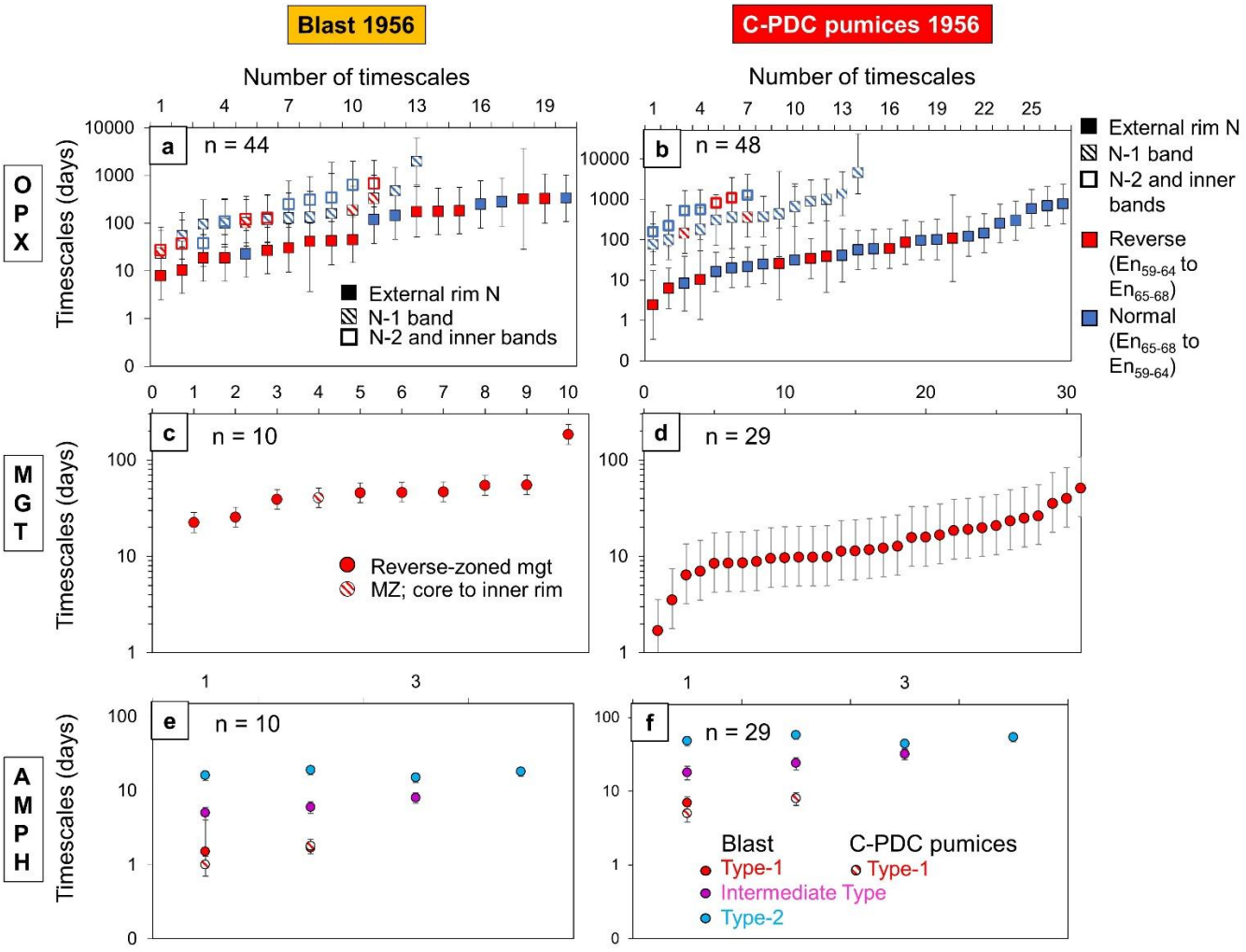


**Supplementary Fig. 13 Individual timescales presented in Fig. 6; Fig. 8-9, modelled in orthopyroxene (opx) (a-b), magnetite (mgt) (c-d) and amphibole crystals (amph) (e-f) and their absolute uncertainties based on the propagation of a temperature uncertainty of ± 50 (for the deep and shallow reservoir temperatures of 850 and 900 °C, respectively) for (a-d) (Martel et al. accepted) or associated with the amphibole rim thicknesses for (e-f)**

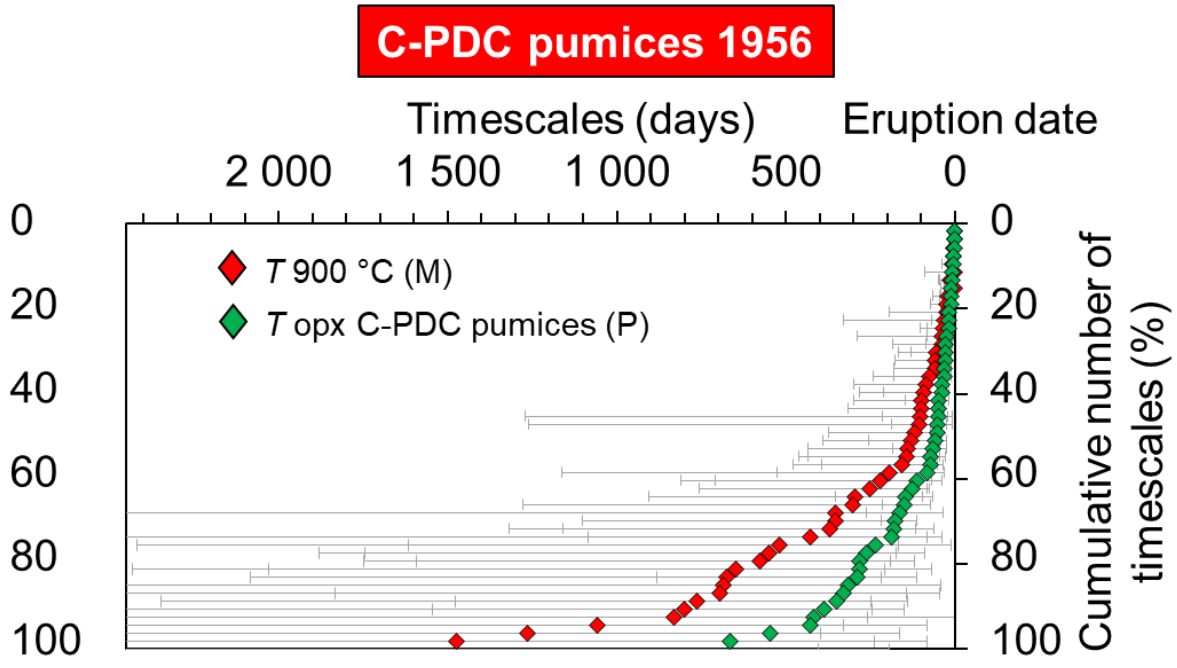


**Supplementary Fig. 14 Comparison of the effects of changes in temperature (*T*) on the timescales modelled for the pumiceous C-PDC. The cumulative number of timescales is shown, according to the timescales (days), and their associated uncertainties. The diffusion coefficient used is from Ganguly and Tazzoli (1994), varying, for the different temperatures summarized in Supplementary Table 2, for the pumiceous C-PDC. The abbreviations used are as follows: M for Martel et al. (accepted), and P for Putirka (2008) (d'Augustin 2021)**

## 3. Supplementary Data

**Supplementary Data 1 AUTODIFF_opx demo to model Fe-Mg diffusion timescales in orthopyroxene crystals. A "Read me" leaflet is inserted to explain how to use the spreadsheet.**

**Supplementary Data 2 AUTODIFF_mgt demo to model Ti diffusion timescales in magnetite crystals. A "Read me" leaflet is inserted to explain how to use the spreadsheet.**

**Supplementary Data 3 Uncertainty calculator used for the orthopyroxene diffusion chronometer, using a Monte-Carlo calculation. Instructions on how to use the spreadsheet are in the first leaflet.**

**Supplementary Data 4 Excel file with whole major element analyses (wt%) of orthopyroxene crystals, En content and Mg number (Mg#) in zoned orthopyroxene crystals of the blast and pumiceous C-PDC of the 1956 eruption of Bezymianny (in the four fractions) and all associated profiles in terms of En content vs distance from the rim (µm), as well as major element analyses (wt%) in unzoned orthopyroxene crystals of the blast and pumiceous C-PDC, En content and Mg number (Mg#). Green lines: lines from which we considered the data to be of good quality. Names of the samples: Bezy 3e, 8f for the blast and Bezy 9 for the pumiceous C-PDC of 1956**

**Supplementary Data 5 Excel file with Fe-Ti magnetite (mgt) profiles in major element analysis (wt%) and the conversions into cationic proportions with $X_{Ti}$. Names of the samples: Bezy 3e, 8f for the blast and Bezy 9 for the pumiceous C-PDC of 1956**

**Supplementary Data 6 Excel file with timescale estimates modelled in AUTODIFF_opx in the zoned orthopyroxene crystals of the blast and pumiceous C-PDC (using the temperatures of Martel et al. (accepted)), with references to the different pathways and En changes recorded. Timescales modelled on compositional profiles are also shown for those in the same magma environments. The fraction in which the orthopyroxene crystals were studied is given (either in 315-500 µm (355), 250-315 µm (250) or 125-250 µm (125)). The uncertainties associated to the timescales are given (negative error, σ- and positive error, σ+). The type of zonation (reverse or normal) is detailed, as well as the position within the orthopyroxene crystals (core to rim (B1 ZS) with ZS indicating single-zoned orthopyroxene crystals or core to first band or outer rims (B1-B8) for multiple-zoned (MZ) orthopyroxene crystals). Model fits for the diffusion timescales of the two samples are also shown, with the intercalibrated data from the EMP and the greyscale and the 1D composition dependent model. All BSE high-resolution images of the corresponding profiles in orthopyroxene zoned crystals measured by EPM and their model fits are shown. The last leaflet shows the timescales correction of the two crystals (one in the blast and one in the pumiceous C-PDC) where inner normal bands where modelled at 850°C and rims at 900°C. Names of the samples: Bezy 3e, 8f for the blast and Bezy 9 for the pumiceous C-PDC of 1956. M is for Martel et al. (accepted), S is for Sauerzapf et al. (2008), G&E is for Ghiorso and Evans (2008) and P is for Putirka (2008) (d'Augustin 2021)**

**Supplementary Data 7 Excel file with timescale estimates modelled in the zoned magnetite crystals of the blast and pumiceous C-PDC using AUTODIFF_mgt. Timescales have been modelled with the temperatures estimated by Martel et al. (accepted) (Supplementary Table 2; Supplementary Fig. 2). All BSE images of the corresponding profiles in magnetite zoned crystals measured by EPM are also shown. Names of the samples: Bezy 3e, 8f for the blast and Bezy 9 for the pumiceous C-PDC of 1956**

## References


Allan ASR, Barker SJ, Millet M-A, et al (2017) A cascade of magmatic events during the assembly and eruption of a super-sized magma body. Contrib to Mineral Petrol 172:49. https://doi.org/10.1007/s00410-017-1367-8

Allan ASR, Morgan DJ, Wilson CJN, Millet M-A (2013) From mush to eruption in centuries: assembly of the super-sized Oruanui magma body. Contrib to Mineral Petrol 166:143–164. https://doi.org/10.1007/s00410-013-0869-2

Aragon R, McCallister RH, Harrison HR (1984) Cation diffusion in titanomagnetites. Contrib to Mineral Petrol 85:174–185. https://doi.org/10.1007/BF00371707

Belousov A (1996) Deposits of the 30 March 1956 directed blast at Bezymianny volcano, Kamchatka, Russia. Bull Volcanol 57:649–662. https://doi.org/10.1007/s004450050118

Belousov A, Voight B, Belousova M (2007) Directed blasts and blast-generated pyroclastic density currents: a comparison of the Bezymianny 1956, Mount St Helens 1980, and Soufrière Hills, Montserrat 1997 eruptions and deposits. Bull Volcanol 69:701–740. https://doi.org/10.1007/s00445-006-0109-y

Belousov AB, Belousova MG (1998) Bezymyannyi Eruption on March 30, 1956 (Kamchatka): Sequence of Events and Debris-Avalanche Deposits. Volcanol Seismol 20:29–47

Boudon G, Balcone-Boissard H, Villemant B, Morgan DJ (2015) What factors control superficial lava dome explosivity? Sci Rep 5:14551. https://doi.org/10.1038/srep14551

Browne B, Gardner J (2006) The influence of magma ascent path on the texture, mineralogy, and formation of hornblende reaction rims. Earth Planet Sci Lett 246:161–176. https://doi.org/10.1016/j.epsl.2006.05.006

Coombs ML, Gardner JE (2004) Reaction rim growth on olivine in silicic melts: Implications for magma mixing. Am Mineral 89:748–758. https://doi.org/10.2138/am-2004-5-608

Costa F, Morgan D (2010) Time Constraints from Chemical Equilibration in Magmatic Crystals. John Wiley & Sons, Ltd, Chichester, UK

Couperthwaite FK, Thordarson T, Morgan DJ, et al (2020) Diffusion timescales of magmatic processes in the Moinui lava eruption at Mauna Loa, Hawai`i, as inferred from bimodal olivine populations. J Petrol 61:1–19. https://doi.org/10.1093/petrology/egaa058

d'Augustin T (2021) Les éléments halogènes dans les magmas, du traçage des conditions de stockage aux flux éruptifs. PhD thesis, Sorbonne Université

Devine JD, Rutherford MJ, Norton GE, Young SR (2003) Magma Storage Region Processes Inferred from Geochemistry of Fe-Ti Oxides in Andesitic Magma, Soufriere Hills Volcano, Montserrat, W.I. J Petrol 44:1375–1400. https://doi.org/10.1093/petrology/44.8.1375

Dias MA, Dohmen R (2024) Experimental determination of Fe–Mg interdiffusion in orthopyroxene as a function of Fe content. Contrib to Mineral Petrol 179:36. https://doi.org/10.1007/s00410-024-02110-7

Dohmen R, Ter heege JH, Becker H-W, Chakraborty S (2016) Fe-Mg interdiffusion in orthopyroxene. Am Mineral 101:2210–2221. https://doi.org/10.2138/am-2016-5815

Fabbro GN, Druitt TH, Costa F (2018) Storage and Eruption of Silicic Magma across the Transition from Dominantly Effusive to Caldera-forming States at an Arc Volcano (Santorini, Greece). J Petrol 58:2429–2464. https://doi.org/10.1093/petrology/egy013

Flaherty T, Druitt TH, Tuffen H, et al (2018) Multiple timescale constraints for high-flux magma chamber assembly prior to the Late Bronze Age eruption of Santorini (Greece). Contrib to Mineral Petrol 173:75. https://doi.org/10.1007/s00410-018-1490-1

Freer R, Hauptman Z (1978) An experimental study of magnetite-titanomagnetite interdiffusion. Phys Earth Planet Inter 16:223–231. https://doi.org/10.1016/0031-9201(78)90015-8

Ganguly J, Tazzoli V (1994) Fe2+-Mg interdiffusion in orthopyroxene: retrieval from the data on intracrystalline exchange reaction. Am Mineral 79:930–937

Gorshkov GS (1959) Gigantic eruption of the volcano bezymianny. Bull Volcanol 20:77–109. https://doi.org/10.1007/BF02596572

Hartley ME, Morgan DJ, Maclennan J, et al (2016) Tracking timescales of short-term precursors to large basaltic fissure eruptions through Fe–Mg diffusion in olivine. Earth Planet Sci Lett 439:58–70. https://doi.org/10.1016/j.epsl.2016.01.018

Higgins O, Sheldrake T, Caricchi L (2022) Machine learning thermobarometry and chemometry using amphibole and clinopyroxene: a window into the roots of an arc volcano (Mount Liamuiga, Saint Kitts). Contrib to Mineral Petrol 177:10. https://doi.org/10.1007/s00410-021-01874-6

Kahl M, Chakraborty S, Costa F, et al (2013) Compositionally zoned crystals and real-time degassing data reveal changes in magma transfer dynamics during the 2006 summit eruptive episodes of Mt. Etna. Bull Volcanol 75:692. https://doi.org/10.1007/s00445-013-0692-7

Kahl M, Chakraborty S, Costa F, Pompilio M (2011) Dynamic plumbing system beneath volcanoes revealed by kinetic modeling, and the connection to monitoring data: An example from Mt. Etna. Earth Planet Sci Lett 308:11–22. https://doi.org/10.1016/j.epsl.2011.05.008

Kilgour GN, Saunders KE, Blundy JD, et al (2014) Timescales of magmatic processes at Ruapehu volcano from diffusion chronometry and their comparison to monitoring data. J Volcanol Geotherm Res 288:62–75. https://doi.org/10.1016/j.jvolgeores.2014.09.010

Krimer D, Costa F (2017) Evaluation of the effects of 3D diffusion, crystal geometry, and initial conditions on retrieved time-scales from Fe–Mg zoning in natural oriented orthopyroxene crystals. Geochim Cosmochim Acta 196:271–288. https://doi.org/10.1016/j.gca.2016.09.037

Mangler MF, Petrone CM, Prytulak J (2022) Magma recharge patterns control eruption styles and magnitudes at Popocatépetl volcano (Mexico). Geology 50:366–370. https://doi.org/10.1130/G49365.1

Martel C, Erdmann S, Boudon G, et al The 1956 eruption of Bezymianny volcano (Kamchatka). Part I - Petrological constraints on magma storage and eruptive dynamics. accepted

Martel C, Pichavant M, Di Carlo I, et al (2021) Experimental Constraints on the Crystallization of Silica Phases in Silicic Magmas. J Petrol 62:. https://doi.org/10.1093/petrology/egab004

Martel C, Pichavant M, Holtz F, et al (1999) Effects of fO2 and H2O on andesite phase relations between 2 and 4 kbar. J Geophys Res Solid Earth 104:29453–29470. https://doi.org/10.1029/1999JB900191

Metcalfe A, Moune S, Komorowski J-C, et al (2021) Magmatic Processes at La Soufrière de Guadeloupe: Insights From Crystal Studies and Diffusion Timescales for Eruption Onset. Front Earth Sci 9:1–28. https://doi.org/10.3389/feart.2021.617294

Morgan DJ, Blake S, Rogers NW, et al (2004) Time scales of crystal residence and magma chamber volume from modelling of diffusion profiles in phenocrysts: Vesuvius 1944. Earth Planet Sci Lett 222:933–946. https://doi.org/10.1016/j.epsl.2004.03.030

Nakamura M (1995) Continuous mixing of crystal mush and replenished magma in the ongoing Unzen eruption. Geology 23:807. https://doi.org/10.1130/0091-7613(1995)023<0807:CMOCMA>2.3.CO;2

Neill OK, Hammer JE, Izbekov PE, et al (2010) Influence of pre-eruptive degassing and crystallization on the juvenile products of laterally directed volcanic explosions. J Volcanol Geotherm Res 198:264–274. https://doi.org/10.1016/j.jvolgeores.2010.09.011

Ostorero L (2022) Spatio-temporal dynamics of the magmatic plumbing systems, towards an « early-warning clock ». Application to Dominica island (Lesser Antilles) and Kamchatka (Russia). Institut de physique du globe de Paris, Université Paris Cité. PhD thesis (476 p).

Ostorero L, Balcone-Boissard H, Boudon G, et al (2022) Correlated petrology and seismicity indicate rapid magma accumulation prior to eruption of Kizimen volcano, Kamchatka. Commun Earth Environ 3:290. https://doi.org/10.1038/s43247-022-00622-3

Ostorero L, Boudon G, Boissard HB, et al (2021) Time - window into the transcrustal plumbing system dynamics of Dominica (Lesser Antilles). Sci Rep 11:1–15. https://doi.org/10.1038/s41598-021-90831-1

Pankhurst MJ, Morgan DJ, Thordarson T, Loughlin SC (2018) Magmatic crystal records in time, space, and process, causatively linked with volcanic unrest. Earth Planet Sci Lett 493:231–241. https://doi.org/10.1016/j.epsl.2018.04.025

Petrone CM, Braschi E, Francalanci L, et al (2018) Rapid mixing and short storage timescale in the magma dynamics of a steady-state volcano. Earth Planet Sci Lett 492:206–221. https://doi.org/10.1016/j.epsl.2018.03.055

Petrone CM, Bugatti G, Braschi E, Tommasini S (2016) Pre-eruptive magmatic processes re-timed using a non-isothermal approach to magma chamber dynamics. Nat Commun 7:12946. https://doi.org/10.1038/ncomms12946

Putirka KD (2008) Thermometers and Barometers for Volcanic Systems. Rev Mineral Geochemistry 69:61–120. https://doi.org/10.2138/rmg.2008.69.3

Rutherford MJ, Devine JD (2003) Magmatic Conditions and Magma Ascent as Indicated by Hornblende Phase Equilibria and Reactions in the 1995-2002 Soufriere Hills Magma. J Petrol 44:1433–1453. https://doi.org/10.1093/petrology/44.8.1433

Rutherford MJ, Hill PM (1993) Magma ascent rates from amphibole breakdown: An experimental study applied to the 1980-1986 Mount St. Helens eruptions. J Geophys Res Solid Earth 98:19667–19685. https://doi.org/10.1029/93JB01613

Saunders K, Blundy J, Dohmen R, Cashman K (2012) Linking Petrology and Seismology at an Active Volcano. Science (80- ) 336:1023–1027. https://doi.org/10.1126/science.1220066

Shcherbakov VD, Neill OK, Izbekov PE, Plechov PY (2013) Phase equilibria constraints on pre-eruptive magma storage conditions for the 1956 eruption of Bezymianny Volcano, Kamchatka, Russia. J Volcanol

Geotherm Res 263:132–140. https://doi.org/10.1016/j.jvolgeores.2013.02.010

Sievwright RH, O'Neill HSC, Tolley J, et al (2020) Diffusion and partition coefficients of minor and trace elements in magnetite as a function of oxygen fugacity at 1150 ºC. Contrib to Mineral Petrol 175:40. https://doi.org/10.1007/s00410-020-01679-z

Solaro-Müller C (2017) Storage conditions and dynamics of magma reservoirs feeding the major pumiceous eruptions of Dominica (Lesser Antilles Arc). University Paris Diderot

Solaro C, Balcone-Boissard H, Morgan DJ, et al (2020) A System Dynamics Approach to Understanding the deep Magma Plumbing System Beneath Dominica (Lesser Antilles). Front Earth Sci 8:. https://doi.org/10.3389/feart.2020.574032

Turner SJ, Izbekov P, Langmuir C (2013) The magma plumbing system of Bezymianny Volcano: Insights from a 54year time series of trace element whole-rock geochemistry and amphibole compositions. J Volcanol Geotherm Res 263:108–121. https://doi.org/10.1016/j.jvolgeores.2012.12.014

Ubide T, Caulfield J, Brandt C, et al (2019) Deep Magma Storage Revealed by Multi-Method Elemental Mapping of Clinopyroxene Megacrysts at Stromboli Volcano. Front Earth Sci 7:239. https://doi.org/10.3389/feart.2019.00239

Venezky DY, Rutherford MJ (1999) Petrology and Fe–Ti oxide reequilibration of the 1991 Mount Unzen mixed magma. J Volcanol Geotherm Res 89:213–230. https://doi.org/10.1016/S0377-0273(98)00133-4

Waters LE, Lange RA (2017) An experimental study of Fe2+-MgKD between orthopyroxene and rhyolite: a strong dependence on H2O in the melt. Contrib to Mineral Petrol 172:42. https://doi.org/10.1007/s00410-017-1358-9